Drag produced by waves trapped at a density interface in non-hydrostatic flow over an axisymmetric hill

Article

Published Version

Drag Produced by Waves Trapped at a Density Interface in Nonhydrostatic Flow over an Axisymmetric Hill

MIGUEL A. C. TEIXEIRA

Department of Meteorology, University of Reading, Reading, United Kingdom

ALEXANDRE PACI AND ANNE BELLEUDY

CNRM, METEO-FRANCE and CNRS (UMR3589), Toulouse, France

(Manuscript received 4 July 2016, in final form 3 March 2017)

ABSTRACT

Linear nonhydrostatic theory is used to evaluate the drag produced by 3D trapped lee waves forced by an axisymmetric hill at a density interface. These waves occur at atmospheric temperature inversions, for example, at the top of the boundary layer, and contribute to low-level drag possibly misrepresented as turbulent form drag in large-scale numerical models. Unlike in 2D waves, the drag has contributions from a continuous range of wavenumbers forced by the topography, because the waves can vary their angle of incidence to match the resonance condition. This leads to nonzero drag for Froude numbers (Fr) both <1 and >1 and a drag maximum typically for Fr slightly below 1, with lower magnitude than in hydrostatic conditions owing to wave dispersion. These features are in good agreement with laboratory experiments using two axisymmetric obstacles, particularly for the lower obstacle, if the effects of a rigid lid above the upper layer and friction are taken into account. Quantitative agreement is less satisfactory for the higher obstacle, as flow nonlinearity increases. However, even in that case the model still largely outperforms both 3D hydrostatic and 2D nonhydrostatic theories, emphasizing the importance of both 3D and nonhydrostatic effects. The associated wave signatures are dominated by transverse waves for Fr lower than at the drag maximum, a dispersive ''Kelvin ship-wave'' pattern near the maximum, and divergent waves for Fr beyond the maximum. The minimum elevation at the density-interface depression existing immediately downstream of the obstacle is significantly correlated with the drag magnitude.

1. Introduction

Topographically forced waves in the atmosphere fall essentially into two categories: vertically propagating or trapped. Vertically propagating waves where the restoring force is gravity have been studied extensively in recent years (Lin 2007; Nappo 2012) in the context of drag parameterization for global weather and climate prediction models. The momentum transported by these waves is deposited in the atmosphere at high levels (McFarlane 1987; Teixeira and Yu 2014), decelerating the mean circulation, an effect that is typically unresolved by those models (Stensrud 2009; Teixeira 2014). The importance of trapped waves propagating at temperature inversions has only been recognized more recently, in particular in connection with the occurrence of lee-wave rotors (Vosper 2004; Hertenstein 2009; Knigge et al. 2010), although early allusions to this kind of waves go back to the pioneering work of Scorer (1949, 1953, 1954). In the ocean, trapped waves are perhaps more familiar, including interfacial waves propagating at the thermocline in flow over submarine ridges and sills (Apel et al. 1985; Farmer and Armi 1999; Cummins et al. 2003), forced by drifting ice keels (Pite et al. 1995) or by ships in the context of the ''dead water'' phenomenon (Grue 2015a), and also, obviously, surface waves propagating at the air–water interface (Phillips 1977), including those generated by ships (Benzaquen et al. 2014; Moisy and Rabaud 2014; Rabaud and Moisy 2014).

In a recent atmospheric study, Teixeira et al. (2013) showed that waves trapped at a temperature inversion (which corresponds to a density interface) produce a drag on 2D topography. This should come as no surprise by analogy with the resistance exerted by internal or

Corresponding author e-mail: Miguel A. C. Teixeira, m.a.teixeira@reading.ac.uk

DOI: 10.1175/JAS-D-16-0199.1

surface waves on vessels (Benzaquen et al. 2014; Rabaud and Moisy 2014; Grue 2015a) or submerged bodies (Tuck 1965). The drag produced by hydrostatic vertically propagating waves in a continuously stratified fluid is especially easy to understand and calculate, forming the basis of current orographic drag parameterizations. However, the mechanisms behind the drag due to waves trapped at low levels in the atmosphere, such as at inversions at the top of the boundary layer, are intrinsically nonhydrostatic (Vosper 2004; Yu and Teixeira 2015), since dispersion is required to produce a spatially extended wavy wake. These waves are forced by relatively narrow mountains, usually poorly represented in large-scale models. Steeneveld et al. (2008) noted that there is currently missing drag in meteorological numerical models, and this deficiency is often alleviated, without a convincing physical justification, by including a so-called long-tail formulation in the form drag parameterization of the turbulent boundary layer [see also Sandu et al. (2013)]. Those authors raise the possibility that this missing drag may be due to unresolved subgrid-scale terrain effects instead. An obvious candidate to account for these effects is the drag associated with trapped lee waves generated over narrow mountains and hills, which, like the turbulent form drag, is also exerted on the atmosphere at low levels. In the present study, this trapped lee-wave drag is investigated theoretically and compared with laboratory experiments, by considering the flow of two fluid layers of different (constant) density over a 3D topography. This setup approximates waves forced by topography at a temperature inversion (in the atmosphere), or waves at the thermocline (in the ocean), forced by, for example, drifting ice keels, ships, or flow over submarine topography (e.g., Pite et al. 1995; Grue 2015a; Farmer and Armi 1999; Bordois et al. 2016). Generically, the applicability of this model to the real atmosphere relies on the dominance of waves that may propagate at the inversion relative to those that may propagate in the layers existing above or below, if any of those are stratified. For a discussion of these conditions, and the effect of stratification aloft on such waves, the reader is referred to a recent study by Sachsperger et al. (2015).

While the drag from waves generated at a free surface in hydrostatic (sometimes called shallow water) flow over 3D topography and nonhydrostatic flow over 2D topography is well known (being given by closed analytical expressions; see Baines 1995), that is not the case with nonhydrostatic flow over 3D topography. The present study proposes deriving an expression for this drag, studying its behavior in parameter space, and comparing it with laboratory experiments carried out in a large water tank following an original idea of E. R. Johnson (University College London). In these experiments, from which results regarding interface displacements were reported by Lacaze et al. (2013), the dependence of the drag on the Froude number (Fr; a key parameter of the flow) is different from that predicted by the theories of hydrostatic flow over 3D topography (where the drag is only nonzero in so-called supercritical conditions, $\mathrm{Fr} > 1$) and nonhydrostatic flow over 2D topography (where, on the contrary, it is only nonzero in subcritical conditions, $\mathrm{Fr} < 1$).

Some previous studies of related problems have considered the shallow-water equations including weak nonlinearity and weak wave dispersion (i.e., nonhydrostatic effects), resulting in a governing equation akin to the Korteweg–de Vries equation (Johnson and Vilenski 2004, 2005; Esler et al. 2007) or arbitrarily strong nonlinearity (Jiang and Smith 2000; Grue 2015b). These studies addressed flow features such as the shape of the wake behind an obstacle and the drag produced by it. They improved the prediction of the latter quantity from hydrostatic (i.e., shallow water) linear theory, among other reasons by avoiding the singular behavior of the drag at $\mathrm{Fr} = 1$, and being able to produce steady waves and nonzero drag for subcritical flow ($\mathrm{Fr} < 1$), as observed experimentally and simulated numerically in fully nonlinear conditions (e.g., Jiang and Smith 2000; Esler et al. 2007; Grue 2015a). However, these authors did not provide a closed-form expression for the drag which could potentially be used with minor adaptations in drag parameterizations. That is one of the aims of the present study. The following calculations will show that inclusion of arbitrarily strong nonhydrostatic and 3D effects is sufficient to produce a very substantial improvement on the predictions from hydrostatic or 2D theory, in fairly good agreement with experimental data, even if the flow is assumed to be strictly linear.

The remainder of this paper is organized as follows. Section 2 describes the linear wave model developed in this study. In section 3, the laboratory experiments are briefly described. Section 4 presents theoretical results, and their comparison with the laboratory experiments, as well as with 3D hydrostatic and 2D nonhydrostatic theories. Finally, in section 5, the main conclusions are summarized and discussed.

2. Theoretical model

Two-layer flow over an axisymmetric obstacle is considered. Each layer is assumed to have constant density: ρ_1 in the lower layer and ρ_2 in the upper one. It is assumed that these densities differ by a small

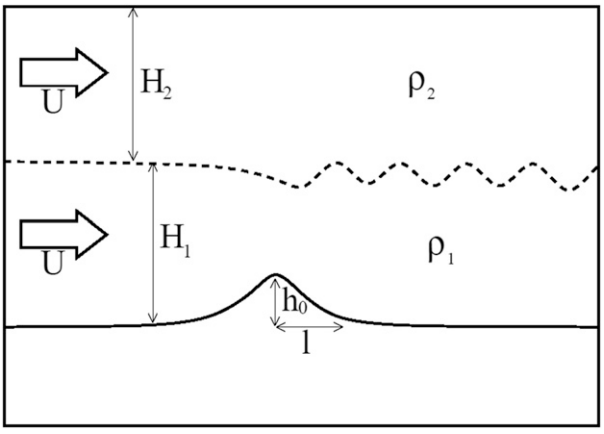

FIG. 1. Profile view of the flow setup considered in the 3D non-hydrostatic linear model developed here. A lower layer, of density ρ_1 and thickness H_1, and an upper layer, of lower density ρ_2 and thickness H_2, flow with a constant incoming velocity U over an axisymmetric hill with maximum height h_0 and half-width l. Stationary resonant (or free) waves at the interface between the two layers are possible if the intrinsic phase velocity of these waves, directed upstream, matches U. This schematic may also represent flow over a 2D obstacle if all represented features are assumed to extend indefinitely in the across-plane direction.

amount, so that they may be approximated without appreciable loss of accuracy by their average value; that is, $\rho_1 \approx \rho_2 \approx \overline{\rho} = (\rho_1 + \rho_2)/2$. The lower layer is assumed to extend from the ground $z = 0$ up to a height $z = H_1$ if undisturbed, while the upper layer is assumed to have a generic thickness H_2, with a rigid lid at its top (see Fig. 1). This configuration is relevant for comparison with the laboratory experiments to be described below, but the model can also be applied to the atmosphere if it is assumed that $H_2 \to \infty$, since the rigid lid is moved to infinity in that case. The undisturbed incoming flow velocity is assumed to be constant in time and space (i.e., the same in both layers), and any effects of the thin boundary layer existing near the ground are neglected (this last assumption will be relaxed, as described in section 2c, strictly for the purpose of comparison with the laboratory experiments).

Subject to these assumptions, the velocity perturbation that is forced as the incoming flow reaches the obstacle is irrotational and stationary. The corresponding velocity potential, denoted by $\phi(x, y, z)$, then satisfies

$$\nabla^2\phi = 0 \tag{1}$$

from mass conservation for an incompressible fluid. Additionally, the Bernoulli equation valid for steady, incompressible flow is

$$\frac{1}{2}\mathbf{v}^2 + \frac{p}{\rho} + gz = \text{const} \tag{2}$$

along a streamline, where $\mathbf{v} = \mathbf{U} + \nabla\phi$ is the total velocity vector, $\mathbf{U}$ is the velocity of the incoming flow, p is the pressure, ρ is the density, g is the acceleration of gravity, and z is height.

Equation (1) must be solved in both layers. If the velocity potential is denoted by ϕ_1 in the lower layer and ϕ_2 in the upper layer, the flow perturbations are assumed to be of relatively small amplitude so that the flow may be linearized, and the incoming flow is assumed to be in hydrostatic equilibrium, the boundary conditions that must be satisfied are

$$\frac{\partial\phi_1}{\partial z}(z = 0) = U\frac{\partial h}{\partial x}, \tag{3}$$

$$\frac{\partial\phi_1}{\partial z}(z = H_1) = \frac{\partial\phi_2}{\partial z}(z = H_1) = U\frac{\partial\eta}{\partial x}, \tag{4}$$

$$\overline{\rho}U\frac{\partial\phi_1}{\partial x}(z = H_1) + \rho_1 g\eta = \overline{\rho}U\frac{\partial\phi_2}{\partial x}(z = H_1) + \rho_2 g\eta, \quad \text{and} \tag{5}$$

$$\frac{\partial\phi_2}{\partial z}(z = H_1 + H_2) = 0, \tag{6}$$

where $h(x, y)$ is the ground elevation (giving the obstacle height) and $\eta(x, y)$ is the vertical displacement of streamlines (or density surfaces) at the interface between the two layers relative to their average height $z = H_1$. Formally, this linearization is valid if $h_0/H_1 \ll 1$, where h_0 is the maximum elevation of the hill. Note that this allows applying the boundary conditions (3)–(5) at the constant coordinates $z = 0$ and $z = H_1$ instead of at the ground and at the perturbed streamline separating the two layers. It is assumed (without loss of generality) that the incoming flow $\mathbf{U} = (U, V)$ is aligned in the x direction; that is, $V = 0$. The first boundary condition (3) expresses free-slip flow at the ground, the second one (4) continuity of the vertical velocity w at $z = H_1$, the third one (5) continuity of the pressure at $z = H_1$, in accordance with a linearized version of (2), and the fourth one (6) no flow across the rigid lid at the top of the domain, $z = H_1 + H_2$. Note that in (5) ρ_1 and ρ_2 have been approximated by $\overline{\rho}$ except in the terms involving gravity. This is equivalent to applying the Boussinesq approximation.

a. Solution procedure

The surface elevation, as well as flow perturbations associated with the waves—namely, ϕ_j (with $j = 1, 2$) and η—are expressed as Fourier integrals along the horizontal directions x and y:

$$h(x, y) = \int_{-\infty}^{+\infty}\int_{-\infty}^{+\infty}\hat{h}(k_x, k_y)e^{i(k_x x + k_y y)}\,dk_x\,dk_y, \tag{7}$$

$$\eta(x,y)=\int_{-\infty}^{+\infty}\int_{-\infty}^{+\infty}\hat{\eta}(k_x,k_y)e^{i(k_xx+k_yy)}\,dk_x\,dk_y, \tag{8}$$

and

$$\phi_j(x,y,z)=\int_{-\infty}^{+\infty}\int_{-\infty}^{+\infty}\hat{\phi}_j(k_x,k_y,z)e^{i(k_xx+k_yy)}\,dk_x\,dk_y,\quad j=1,2, \tag{9}$$

where $i=\sqrt{-1}$, (k_x, k_y) is the horizontal wavenumber vector, and the hat denotes Fourier transform.

If (9) is inserted into (1), the corresponding solutions for $\hat{\phi}_j$ in the two layers are

$$\hat{\phi}_1=a_1e^{-\kappa z}+b_1e^{\kappa z}\quad\text{and} \tag{10}$$

$$\hat{\phi}_2=a_2e^{-\kappa z}+b_2e^{\kappa z}, \tag{11}$$

where $\kappa=(k_x^2+k_y^2)^{1/2}$ is the magnitude of the horizontal wavenumber and the coefficients a_1, b_1, a_2, and b_2 are functions of (k_x, k_y) to be determined. If the boundary conditions (3)–(6) are applied to these solutions, it is possible to determine these coefficients as a function of $\hat{h}$ and $\hat{\eta}$, the latter of which can also be expressed in terms of $\hat{h}$. Thus,

$$a_1=\frac{iUk_x(\hat{\eta}-\hat{h}e^{\kappa H_1})}{2\kappa\sinh(\kappa H_1)},\quad b_1=\frac{iUk_x(\hat{\eta}-\hat{h}e^{-\kappa H_1})}{2\kappa\sinh(\kappa H_1)}, \tag{12}$$

$$a_2=-\frac{iUk_x\hat{\eta}e^{\kappa(H_1+H_2)}}{2\kappa\sinh(\kappa H_2)},\quad b_2=-\frac{iUk_x\hat{\eta}e^{-\kappa(H_1+H_2)}}{2\kappa\sinh(\kappa H_2)},\quad\text{and} \tag{13}$$

$$\hat{\eta}=\frac{U^2k_x^2\hat{h}}{\sinh(\kappa H_1)\{U^2k_x^2[\coth(\kappa H_1)+\coth(\kappa H_2)]-g'\kappa\}}, \tag{14}$$

where $g'=g|\rho_1-\rho_2|/\overline{\rho}$ is the reduced gravity of the interface existing between the two layers at $z=H_1$.

b. Wave drag

The primary aim here is to evaluate the surface drag produced by the waves. This is given by

$$D=\int_{-\infty}^{+\infty}\int_{-\infty}^{+\infty}p'(z=0)\frac{\partial h}{\partial x}\,dx\,dy$$

$$=8\pi^2\mathrm{Im}\left[\int_{-\infty}^{+\infty}\int_{0}^{+\infty}k_x\hat{p}'(z=0)\hat{h}^*\,dk_x\,dk_y\right], \tag{15}$$

where p' is the pressure perturbation and $\hat{p}'$ its Fourier transform, and the asterisk denotes complex conjugate. The drag only has an x component, since the topography is assumed to be axisymmetric (as will be defined) and the wind velocity is along x. In the second equality of (15), use was made of Parseval's theorem and of the fact that p', h, and D are real quantities.

From a linearized version of (2), along with (10), the Fourier transform of the pressure perturbation at the surface may be written

$$\hat{p}'(z=0)=-i\rho_1Uk_x(a_1+b_1)=\rho_1U^2k_x^2\frac{\hat{\eta}-\hat{h}\cosh(\kappa H_1)}{\kappa\sinh(\kappa H_1)}, \tag{16}$$

where, in the second equality, (12) has been used. It can be easily seen that, when (16) is inserted into (15), since the term involving $\hat{h}$ is real and has no singularities, it cannot contribute to the imaginary part of the integral in (15). Hence, only the term involving $\hat{\eta}$ in (16) can contribute to the drag. Taking this into account, and using also (14), it can be shown that (15) may be expressed as

$$D=16\pi^2\rho_1U^2\mathrm{Im}\left\{\int_0^{+\infty}\int_0^{+\infty}\frac{k_x^5|\hat{h}(k_x,k_y)|^2}{\kappa\sinh^2(\kappa H_1)}\times\frac{1}{k_x^2[\coth(\kappa H_1)+\coth(\kappa H_2)]-(g'/U^2)\kappa}\,dk_x\,dk_y\right\}, \tag{17}$$

where the fact that the integrand is symmetric with respect to k_y (the wavenumber in the y direction) has been used. It is now convenient to introduce polar coordinates, where $k_x=\kappa\cos\theta$ and $k_y=\kappa\sin\theta$. In terms of these coordinates, (17) becomes

$$D=16\pi^2\rho_1U^2h_0^2\left(\frac{l}{\overline{H}}\right)^4\mathrm{Im}\left\{\int_0^{+\infty}\int_0^{\pi/2}\frac{\kappa'^4\cos^5\theta|\hat{h}'(\kappa')|^2}{\sinh^2(\kappa'H_1')}\times\frac{1}{\kappa'\cos^2\theta[\coth(\kappa'H_1')+\coth(\kappa'H_2')]-\mathrm{Fr}^{-2}}\,d\theta\,d\kappa'\right\}, \tag{18}$$

where $\overline{H}=H_1H_2/(H_1+H_2)$ is a weighted thickness of the two fluid layers, $H_1'=H_1/\overline{H}$, $H_2'=H_2/\overline{H}$, $\kappa'=\kappa\overline{H}$ is a dimensionless wavenumber, and $\hat{h}'=\hat{h}/(h_0l^2)$ is a dimensionless Fourier transform of the terrain elevation, normalized using the height of the obstacle h_0 and its width l. The Froude number $\mathrm{Fr}=U/(g'\overline{H})^{1/2}$ quantifies the ratio between the mean-flow speed and the phase speed of shallow-water waves at the interface separating the two fluid layers. Note that, since the mountain is assumed to be axisymmetric, $\hat{h}$ does not depend on θ, and thus may be moved outside the integral in θ. This is one of the reasons for using polar coordinates in

(18). Since the integrand in (18) is real, any contribution to the drag must come from singularities when the denominator of the fraction in the second line of this equation is zero. These singularities, which correspond to resonant wave modes, are given by the condition

$$\cos^2\theta_R = \frac{\mathrm{Fr}^{-2}}{\kappa'[\coth(\kappa' H_1') + \coth(\kappa' H_2')]}, \tag{19}$$

where θ_R denotes the resonant azimuthal wavenumber angle. These waves travel, in general, at an angle to the mean flow, as is observed in ship waves and trapped lee waves over 3D mountains (Wurtele et al. 1996), because that is the way they can oppose the mean flow exactly (so as to become steady) even when their phase speed does not match the incoming wind speed. This angle is explicitly given by (19) as a function of κ', and that is another reason for having adopted polar coordinates. If (19) is satisfied, the integral over θ in (18) may be calculated using complex integration (see appendix), and its only imaginary contribution comes from the singularity defined by (19). After some algebra, this yields

$$D = 8\pi^3 \rho_1 g' l h_0^2 \mathrm{Fr}^{-2} \left(\frac{l}{\overline{H}}\right)^3 \int_0^{+\infty} \frac{\kappa' [\hat{h}'(\kappa')]^2}{\sinh^2(\kappa' H_1')} \times \frac{1}{[\coth(\kappa' H_1') + \coth(\kappa' H_2')]^3 \left\{1 - \dfrac{\mathrm{Fr}^{-2}}{\kappa'[\coth(\kappa' H_1') + \coth(\kappa' H_2')]}\right\}^{1/2}} d\kappa', \tag{20}$$

where (19) has been used to eliminate θ_R. Note that (20) is only valid when the term in the curly brackets in the denominator is positive. This corresponds to having the right-hand side of (19) less than or equal to 1, as must be for resonant wave modes to be possible. These resonant wave modes correspond to free waves that are able to be sustained in a steady-state flow. The component of the incoming flow perpendicular to the phase lines of these waves $U\cos\theta_R$ is equal and opposite to their intrinsic phase velocity. If this condition is not satisfied, then no resonant wave modes exist and $D = 0$.

Equation (20) is the main theoretical result of this study. In what follows, the drag is normalized by $\rho_1 g' l h_0^2$ [as done by, e.g., Jiang and Smith (2000) and Esler et al. (2007)], because this choice reduces the number of input parameters of the theoretical model to a minimum. A requirement for this to happen is that the normalizing factor is proportional to h_0^2, because this eliminates the dependence of the normalized drag on mountain height, which should not exist in a linearized framework. Note that although this choice is the best one for making comparisons with linear theory, it may not give the best scaling for the drag when nonlinear effects are important (as will be seen).

With this choice, the drag depends on three dimensionless parameters: Fr, l/H_1, and H_1/H_2. The physical meaning of Fr was already mentioned, and l/H_1 quantifies nonhydrostatic effects. When $l/H_1 \to \infty$, the flow is hydrostatic or "shallow water." It might be argued that $l/\overline{H}$ should be used instead of l/H_1, since it appears explicitly in (20); however, l/H_1 is preferred here instead because it can be calculated more directly from basic parameters of the flow. Note also that l/H_1 and H_1/H_2 appear implicitly in $\hat{h}$, since this is provided in the form $\hat{h}(l\kappa)$ (as will be seen in the next section), and this dependence can also be expressed as $\hat{h}(\kappa', l/H_1, H_1/H_2)$ because of the definition of κ'. It can be easily shown that H_1' and H_2' are exclusive functions of H_1/H_2. Finally, note that, unlike what happens in 2D trapped lee waves, the drag in (20) receives contributions from a range of wavenumbers, so it is influenced by the shape of the orography in its entirety, instead of only by a single harmonic (as happens in 2D flow; e.g., Teixeira et al. 2013).

The case most relevant to the atmosphere is that where the upper layer becomes infinitely thick, $H_2 \to \infty$. Then $\overline{H} = H_1 H_2/(H_1 + H_2) \approx H_1$, $H_1' \approx 1$, $H_2' \to \infty$, and consequently (20) becomes

$$D = 8\pi^3 \rho_1 g' l h_0^2 \mathrm{Fr}^{-2} \left(\frac{l}{H_1}\right)^3 \int_0^{+\infty} \frac{\kappa' \sinh\kappa' |\hat{h}'(\kappa')|^2}{(\cosh\kappa' + \sinh\kappa')^3 \left[1 - \dfrac{\mathrm{Fr}^{-2}\sinh\kappa'}{\kappa'(\cosh\kappa' + \sinh\kappa')}\right]^{1/2}} d\kappa'. \tag{21}$$

When additionally the flow is hydrostatic, which corresponds to assuming in (21) that $\kappa' \to 0$, and therefore $\sinh\kappa' \approx \kappa' \approx 0$ and $\cosh\kappa' \approx 1$, (21) reduces to

$$D = 8\pi^3 \rho_1 g' l h_0^2 \left(\frac{l}{H_1}\right)^3 \frac{\mathrm{Fr}^{-2}}{(1-\mathrm{Fr}^{-2})^{1/2}} \int_0^{+\infty} \kappa'^2 |\hat{h}'(\kappa')|^2 \, d\kappa', \tag{22}$$

as noted by Baines (1995) or Jiang and Smith (2000). This equation clearly shows that, in this limit, wave drag only exists for supercritical flow, $\mathrm{Fr} > 1$, as is well known. That does not happen when the flow is nonhydrostatic, as can be inferred from (19) and will be illustrated in section 4.

An analogous procedure may be used to calculate the resonant component of η, denoted η_R, which should dominate the flow downstream of the obstacle. Using also complex integration to eliminate the integral along the azimuthal angle θ, as in (21), η_R normalized by h_0 in the $H_2 \to \infty$ limit is found to take the form

$$\begin{aligned}\frac{\eta_R(x,y)}{h_0} = -2\pi \left(\frac{l}{H_1}\right)^2 \int_0^{+\infty} & \frac{\kappa' \cos\theta_R \hat{h}'(\kappa')}{\sin\theta_R(\cosh\kappa' + \sinh\kappa')} \\ & \times \{\sin[\kappa'(x'\cos\theta_R + y'\sin\theta_R)] \\ & + \sin[\kappa'(x'\cos\theta_R - y'\sin\theta_R)]\} \, d\kappa', \end{aligned} \tag{23}$$

where $x' = x/H_1$, $y' = y/H_1$, and both $\cos\theta_R$ and $\sin\theta_R$ can be obtained from (19) evaluated in the same limit. In the second and third lines of (23), it is clear that η_R contains waves that are oblique in the x–y plane and symmetric with respect to $x = 0$, which is consistent with a "ship wave" pattern. In what follows, η_R is only going to be analyzed for $H_2 \to \infty$, as this is the situation most relevant to the atmosphere.

c. *Inclusion of friction*

To compare the drag predictions produced by the present model with those of the laboratory experiments to be described next, it is necessary to consider the effects of friction. The simplest possible way of doing this is by incorporating friction as a Rayleigh damping acting on the flow. A slightly more elaborate choice would be including a bulk representation of the boundary layer, as developed by Smith et al. (2006) and Smith (2007). This latter approach, which was followed recently by Teixeira (2017) in the context of trapped lee-wave rotors, however adds three new input parameters to the model described previously. Tests with both approaches show that the added complexity of the bulk boundary layer approach does not translate into an improvement in the performance of the model (as quantified in the comparisons of section 4b); therefore, the Rayleigh damping approach, which only has one additional input parameter, is adopted. This can be accomplished by changing the boundary condition based on the Bernoulli equation, (5), to

$$\begin{aligned}\overline{\rho}\left[U\frac{\partial \phi_1}{\partial x}(z=H_1) + \lambda\phi_1(z=H_1)\right] + \rho_1 g\eta \\ = \overline{\rho}\left[U\frac{\partial \phi_2}{\partial x}(z=H_1) + \lambda\phi_2(z=H_1)\right] + \rho_2 g\eta,\end{aligned} \tag{24}$$

where λ is the Rayleigh damping coefficient. This approach, where friction is applied globally, accounts for all possible sources of friction occurring in the experiments. If (24) is implemented in the model, (12) and (13) remain unchanged, but (14) is modified to

$$\hat{\eta} = \frac{U^2 k_x^2 \hat{h}[1 - i\lambda/(Uk_x)]}{\sinh(\kappa H_1)\{U^2 k_x^2[1 - i\lambda/(Uk_x)][\coth(\kappa H_1) + \coth(\kappa H_2)] - g'\kappa\}}. \tag{25}$$

This will lead to a more complicated expression for the drag than (20) (which is omitted here), involving a double integral in both κ and θ, since the singularity in (18) is moved away from the real axis by friction, and hence the integral in θ may not be eliminated using contour integration (as done previously). All results including friction will use this drag expression, which, as the integrals in (20)–(23), is evaluated using numerical integration. Note that the only additional dimensionless input parameter that accounts for friction is $\lambda\overline{H}/U$, whose value will be adjusted to optimize the results.

3. Laboratory experiments

The experiments were performed in the large stratified water flume at the Geophysical Fluid Mechanics Laboratory of CNRM in Toulouse, upon an original idea of E. R. Johnson (University College London). This laboratory has been used in the recent past to study a wide range of stratified flows in a geophysical context, from oceanic tides (e.g., Dossmann et al. 2011; Dossmann et al. 2014) to atmospheric stable boundary layers and orographic waves (e.g., Knigge et al. 2010).

The flume was used here as a 22-m-long, 3-m-wide, and 1-m-high towing tank. The tank was filled with a stratified two-layer fluid made of saline water using a special procedure to ensure a sharp density interface between the two layers.

Two axisymmetric obstacles, referred to herein as obstacle A and obstacle B, of base diameter 100 cm and maximum heights $h_0 = 7.7$ and 12.5 cm, respectively, were towed at the surface of the tank at several constant speeds U in the range 5–33 cm s^{-1}, allowing the achievement of different Froude numbers. For this two-layer fluid, the Froude number is defined as in the theoretical model described in section 2:

$$\mathrm{Fr} = \frac{U}{\sqrt{g'\overline{H}}}. \tag{26}$$

Also as in the model, H_1 is the depth of the layer in direct contact with the obstacle (typically $H_1 = 15$ cm), and H_2 is the depth of the other layer (farther from the obstacle), with a value close to H_1 or slightly larger (the total depth $H_1 + H_2 \approx 31$ cm is fixed). But, in contrast with the model and with Fig. 1, the first layer is above the second, so layer 1 (of typical density $\rho_1 \approx 1000$ kg m^{-3}) is the least dense one in the experiments ($\rho_2 \approx 1059$ kg m^{-3}). This detail makes no significant difference in the Boussinesq approximation framework that applies here, as the density discontinuity between the two layers $\Delta\rho = |\rho_1 - \rho_2|$ is small relative to $\overline{\rho}$ ($\Delta\rho/\overline{\rho} \approx 6 \times 10^{-2}$). The radial profile of the obstacles, which is also adopted in the model calculations, is given by

$$h(r) = h_0 \exp(-2r^2/l^2), \tag{27}$$

where $r = (x^2 + y^2)^{1/2}$ [the obstacle being centered at $(x = 0, y = 0)$] and $l = 32$ cm is defined as $l = 2\sigma$, where σ is the standard deviation of the Gaussian function, corresponding to a characteristic horizontal length scale of the obstacle. The Fourier transform of the obstacle elevation then takes the form

$$\hat{h}(\kappa) = \frac{h_0 l^2}{8\pi}\exp\left(-\frac{1}{8}l^2\kappa^2\right)$$

$$\Rightarrow \quad \hat{h}' = \frac{1}{8\pi}\exp\left\{-\frac{1}{8}\kappa'^2\left[\frac{l}{H_1}\left(1+\frac{H_1}{H_2}\right)\right]^2\right\}, \tag{28}$$

which is used in all model calculations.

The flow configuration is equivalent to that shown in Fig. 1 turned upside down, with the ground replaced by the free surface of the upper fluid layer, and the frame of reference traveling with the flow. Note that, because the obstacle is the only solid boundary moving relative to layer 1, the boundary layer develops only on the obstacle and is therefore less developed than if a solid surface extended over the whole boundary. In other words, the boundary condition is no slip only on the obstacle and free slip elsewhere.

Measurements combined an optical stereoscopic method to retrieve the interface shape [reported in Lacaze et al. (2013)] and a force measurement on the obstacle being towed to estimate the drag. More specifically, drag measurements were carried out using a strain gauge able to measure a force in the range from 20 mN to 20 N with a resolution of 10 mN and a data acquisition rate of 1 Hz. Data were first filtered by removing values differing from the average by more than 1.96 times the standard deviation. The estimate of the drag was then obtained by averaging the remaining data excluding the transient periods that comprise the towing bank acceleration time necessary to attain a constant speed and the deceleration time from a constant speed to zero. Error bars are the 90% confidence interval computed from bootstrap resampling. More details regarding the experiments can be found in Lacaze et al. (2013).

Laboratory experiments are particularly appropriate to evaluate a theoretical model, as they represent a real flow, but with highly controlled conditions. To be representative of the geophysical flows they intend to simulate, laboratory experiments must be in a flow regime similar to the corresponding atmospheric or oceanic flows. This requires first of all having density stratification effects and high Reynolds numbers in the laboratory experiments. These conditions are rarely met simultaneously in the same facility, but the CNRM large stratified water flume in Toulouse was designed specifically for this purpose. In addition, the relevant dimensionless parameters controlling the physics of the problem must be similar. This means that the key parameters (such as Fr in the present case) need to be equal, whereas it is enough for other parameters to be above (or below) a given threshold (e.g., the Reynolds number in the present case).

4. Results

a. Behavior of the normalized drag

First of all, the drag behavior produced by the theoretical model described in section 2 is explored in the inviscid limit as a function of the input parameters H_1/H_2, l/H_1, and Fr. Figure 2 shows the normalized drag as a function of Fr for different values of l/H_1 and three representative values of H_1/H_2. Figure 2a corresponds to $H_1/H_2 = 0$, the case most relevant to the atmosphere, Fig. 2c to $H_1/H_2 = 1$, a case where the finite thickness of

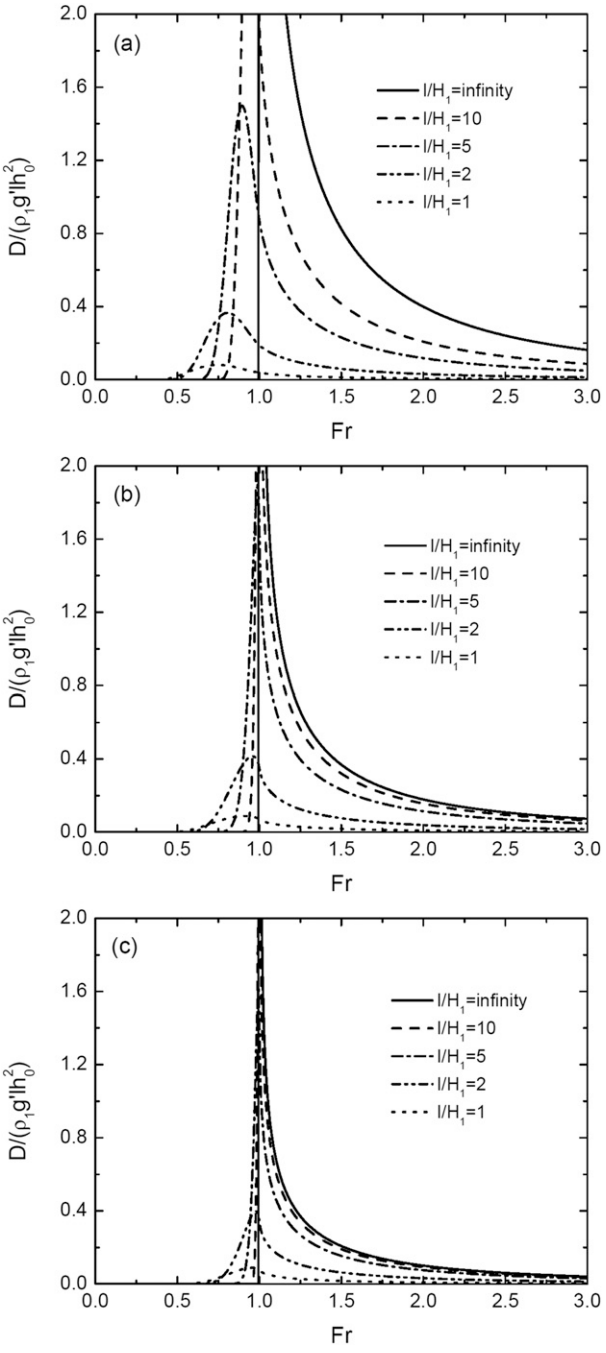

FIG. 2. Drag from (20) normalized by $\rho_1 g' l h_0^2$ as a function of Fr for different values of l/H_1 (which controls nonhydrostatic effects—see legend) and H_1/H_2 (which controls the relative thickness of the two layers). The condition $l/H_1 = \infty$ corresponds to hydrostatic (shallow water) flow (where the drag is zero for Fr < 1), and $H_1/H_2 = 0$ to an infinitely thick upper layer. (a) $H_1/H_2 = 0$, (b) $H_1/H_2 = 0.5$, (c) $H_1/H_2 = 1$.

the upper layer affects the flow in a way not too different from that produced in the experiments, and Fig. 2b to an intermediate situation ($H_1/H_2 = 0.5$). The drag has a strong variation with Fr, approaching zero at low and high Fr and attaining a maximum near Fr ≈ 1. This is reminiscent of the drag behavior in Teixeira et al. (2013), although in that 2D geometry the trapped lee-wave drag for Fr > 1 was zero. This no longer happens for the 3D geometry considered here, because the waves have the additional degree of freedom of being able to vary their incidence angle to satisfy the resonance condition over the whole range of variation of Fr (except for Fr < 1 in the limit of perfectly hydrostatic flow, as explained below).

For hydrostatic flow ($l/H_1 = \infty$), the drag is only nonzero for Fr ≥ 1, in accordance with (22). This situation corresponds to shallow-water waves propagating at a constant angle to the incoming flow, so that the projection of their phase along x allows U to match the corresponding intrinsic phase speed $c_s = (g'\overline{H})^{1/2}$. As shown by Fig. 3, this occurs only when Fr ≥ 1, because $U > c_s$ is then a necessary condition for steady waves. The infinite value of the drag that occurs at Fr $= 1$ corresponds to waves with phase velocity aligned with the incoming flow and is obviously an artifact of the linear and inviscid approximations, which for these conditions break down.

As the flow becomes more nonhydrostatic (i.e., l/H_1 decreases), the normalized drag decreases globally in magnitude but becomes nonzero for Fr < 1, attaining its maximum for a value of Fr slightly lower than 1. This translation of the drag maximum to lower Fr is especially pronounced for $H_1/H_2 = 0$ (Fig. 2a), and less significant for $H_1/H_2 = 1$ (Fig. 2c), probably because the finite extent of the upper layer makes the flow more hydrostatic (shallow water) than when that layer extends indefinitely. Not surprisingly, the fact that the drag is nonzero for Fr < 1 is due to nonhydrostatic effects. This can be understood most easily if we look now at Fig. 1 as portraying a 2D situation, where resonant waves can only propagate in the x direction. Since the intrinsic phase speed c of nonhydrostatic waves is smaller than that of hydrostatic (shallow water) waves c_s (i.e., $c < c_s$) and the former speed must be matched by the mean flow speed U in order for the waves to be stationary, this requires that Fr $= U/c_s = c/c_s \leq 1$. This argument applies not only to pure interfacial waves (Baines 1995), but also to those influenced by continuous stratification aloft, as in Teixeira et al. (2013). For waves at different incidence angles, the resonance condition can also be fulfilled for Fr > 1, as in hydrostatic conditions. The fact that the drag maximum occurs for lower Fr as nonhydrostatic effects increase is a joint

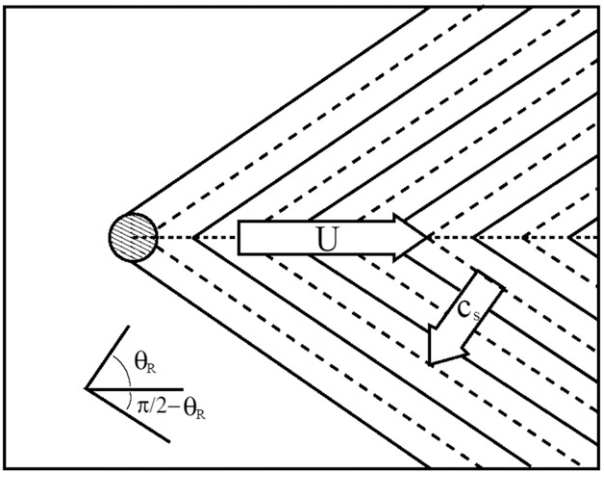

FIG. 3. Plan view of stationary interfacial waves in hydrostatic (shallow water) flow over a 3D obstacle. Resonant or free steady waves (those that produce drag) are possible if the angle θ_R between the intrinsic shallow-water phase velocity, with value $c_s = (g'\overline{H})^{1/2}$, and the wind velocity U is such that $\cos\theta_R = c_s/U$. From the definition of Froude number $\mathrm{Fr} = U/c_s$, this necessarily corresponds to $\mathrm{Fr} \geq 1$.

effect of the ability to have stationary waves for $\mathrm{Fr} < 1$ (as seen above) and existence of sufficient forcing at the corresponding resonant wavenumbers, provided by the orography.

The drag becomes generally lower as l/H_1 decreases as a result of a decreasing height or depth of penetration of the waves—that is, the vertical distance over which the orbital motions of the waves decay (which is infinite for hydrostatic or shallow-water flow). As this distance becomes a smaller fraction of H_1, the interaction between the waves at $z = H_1$ and the topography progressively weakens. The fact that the drag maximum becomes finite at $\mathrm{Fr} = 1$ and there is nonzero drag for subcritical flow ($\mathrm{Fr} < 1$) are intrinsic features of 3D nonhydrostatic theory, associated with wave dispersion (or nonhydrostatic/deep-water effects), which bring it in closer agreement to both the present measurements (as shown next) and those by previous authors (e.g., Pite et al. 1995). By decreasing the amplitude of the wave perturbation relative to hydrostatic flow, dispersion also necessarily extends the range of applicability of linear theory to larger obstacle heights.

b. Comparison with experimental data

The model described in section 2 is now compared with the experiments described in section 3. As will be seen, nonlinear processes seem to be relatively modest for obstacle A but more important for obstacle B. The balance between nonlinear and nonhydrostatic effects [as assumed in Esler et al. (2007)] might provide a better description of the flow in the latter case, as will be speculated below.

Figure 4 shows the normalized drag calculated from (20) with Rayleigh friction included (solid lines and filled circles) and from the measurements (open circles with error bars) for the lower obstacle A (Figs. 4a,c,e) and for the higher obstacle B (Figs. 4b,d,f). For comparison, the dashed–dotted lines and stars correspond to the model (without friction) where $H_2 \to \infty$ is assumed (21), the dashed–double-dotted lines correspond to (20) (without friction), the dotted lines correspond to results from inviscid 3D hydrostatic theory (22), and the dashed lines correspond to results from inviscid 2D nonhydrostatic theory, equivalent to those produced by the model of Teixeira et al. (2013) when the stratification of the upper layer is zero. Note that the 2D drag is expressed per unit length, and so has different units to the 3D drag, hence it is normalized here by $\rho_1 g' l h_0^2$ instead of $\rho_1 g' l h_0^2$.

For all theoretical results, the symbols correspond to drag values where the value of each model input parameter was taken from the experiments point by point, whereas the lines show the variation of the drag with Fr for averaged values of the other input parameters. No symbols were included along with the dotted, dashed, and dashed–double-dotted lines because those symbols would follow the lines fairly closely but also make the graphs too confusing.

In Figs. 4a,b the experimental data use the default definition of the Froude number based on an infinitely thin density-interface approximation (26). In Figs. 4c–f, on the other hand, Fr values that were corrected for the real finite thickness of the interface were used in the experimental data. Since this procedure allows a more accurate estimate of the phase speed of the waves trapped at the interface, which is crucial for defining a physically meaningful Froude number, it should provide a better comparison with the model developed here. In Figs. 4a,b both the model results and the data use the Fr values given by the default definition; in Figs. 4c,d the data use the corrected Fr values, whereas the model results use the default definition (which is consistent with the model's assumptions). This should provide the fairest comparison. However, the fact that in this case the model and the data use different values of Fr precludes a comparison of the drag point by point. To avoid this, in Figs. 4e,f corrected Fr values are used both in the data and in the model, keeping all other input parameters unchanged.

In all model results with friction displayed in Fig. 4, the Rayleigh damping parameter was adjusted to produce the best possible agreement of the drag between

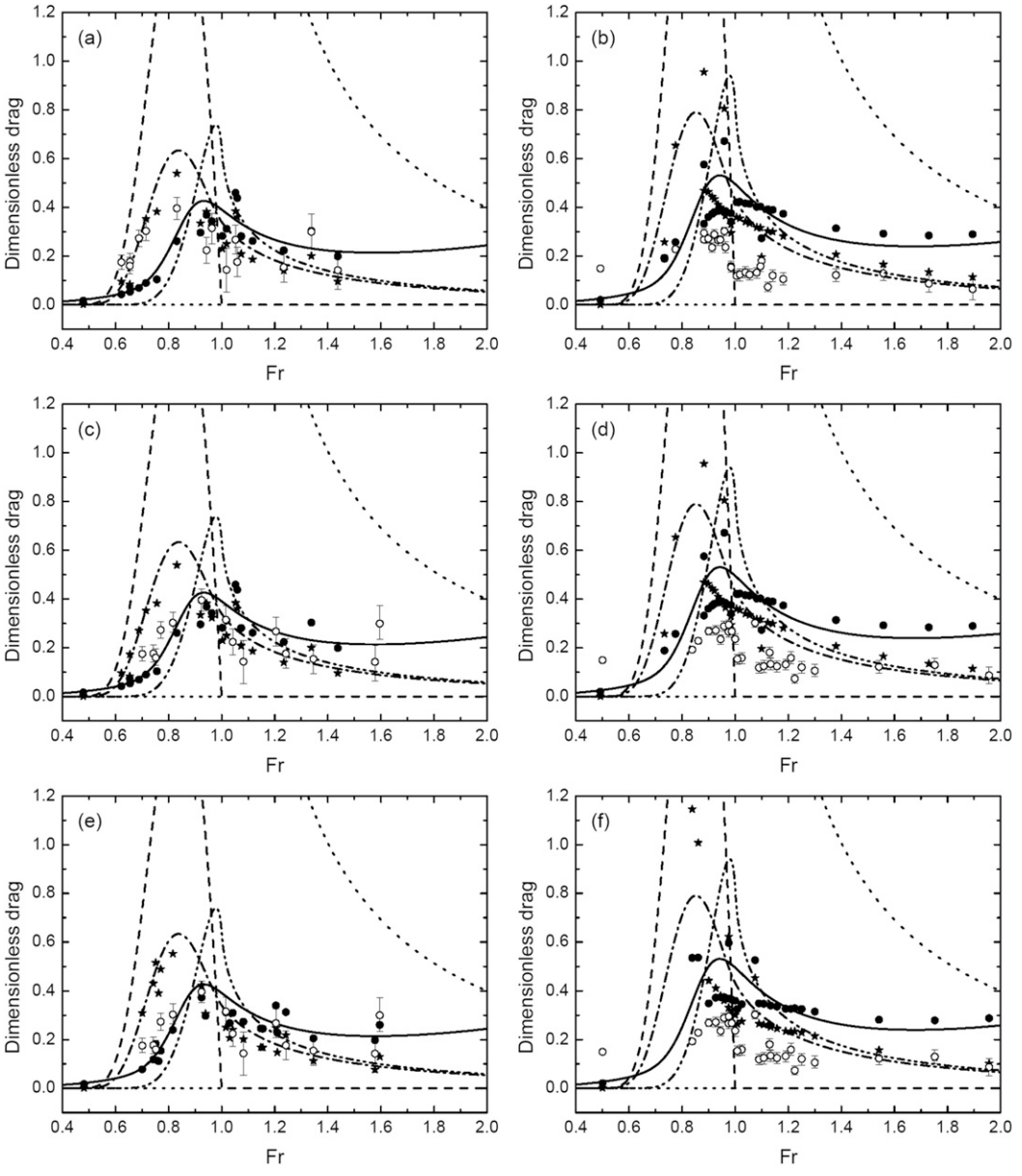

FIG. 4. Comparison of the normalized drag between experimental data (open circles with error bars) and 3D nonhydrostatic two-layer theory (20) including friction (solid lines and filled circles), inviscid 3D hydrostatic theory (22) (dotted lines), inviscid 2D nonhydrostatic theory (dashed lines), inviscid 3D nonhydrostatic theory for $H_2 \to \infty$ (21) (dashed–dotted lines and stars), and inviscid 3D nonhydrostatic two-layer theory (20) (dashed–double-dotted lines). The symbols use parameter values Fr, l/H_1, and H_1/H_2 from the experiments for each data point, whereas the lines use averaged values of l/H_1 and H_1/H_2. (a),(b) Default Fr definition (26) used in both theory and data; (c),(d) default Fr definition used in theory and corrected Fr used in data; (e),(f) corrected Fr used in both theory and data. (a),(c),(e) Lower obstacle A: averaged values of $M = 0.66$, $l/H_1 = 2.73$, and $H_1/H_2 = 0.64$ from measurements assumed in lines; (b),(d),(f) higher obstacle B: averaged values of $M = 1.12$, $l/H_1 = 3.14$, and $H_1/H_2 = 0.52$ from measurements assumed in lines.

model and experimental data for obstacle A, taking the value $\lambda\overline{H}/U = 0.06$.

Given the measurement error bars, and the numerous assumptions in the model that are not strictly or even approximately satisfied, the agreement is surprisingly good in Figs. 4a,c,e (obstacle A). In Fig. 4a, the two-layer model with friction (solid line and filled circles) predicts the magnitude of the drag maximum accurately (which is not surprising, since the friction coefficient was adjusted to achieve this),

while the model for $H_2 \to \infty$ without friction (dashed–dotted line and stars) slightly overestimates this maximum but predicts better its location in terms of Fr, as well as the drag to the left of this maximum. The two-layer model without friction (dashed–double-dotted line) overestimates both the drag maximum and the value of Fr at which it occurs. The effect of friction is primarily lowering the drag maximum, broadening it as a function of Fr, and moving it to lower Fr, which corresponds to a frictional decrease of the phase speed of the waves (supported by previous studies; e.g., Hunt 1964).

Figure 4c shows that when the Fr used in the experimental data is the corrected one, agreement with the two-layer model including friction improves very substantially, and becomes unquestionably the best one. This agreement is preserved in Fig. 4e, where the model also uses the corrected Fr values. Since the values of H_1/H_2 and l/H_1 are unchanged from Fig. 4c, the same dependence on Fr is retained, while allowing a more detailed comparison to be made point by point. In both cases (Figs. 4c,e), despite the data scatter, there is still a slight tendency to underestimate the drag to the left of its maximum and overestimate it to the right of the maximum, which may be due to nonlinearity (cf. Fig. 3 of Grue 2015b). However, the drag values predicted by the two-layer model with friction in Fig. 4e are typically within a factor of 2 of the experimental data. Among the 14 data points available from the experiments, in 13 of them (93%) the model results differ from the data by a factor no larger than 2, 6 points (43%) are within the error bars, and 11 points (79%) are within twice the error bars. The average ratio between the theoretical and the experimental drag values is 1.10.

The nonzero values of the drag for $\mathrm{Fr} < 1$ and drag maximum existing at $\mathrm{Fr} \approx 0.9$ are well reproduced. The model also seems to capture quite well the nonzero values of the drag to the right of the main maximum (e.g., at $\mathrm{Fr} \approx 1.6$), which may be interpreted physically as being due to frictional effects [cf. Figs. 9 and 10 of Pite et al. (1995) for a similar drag behavior]. An estimate of frictional effects even more simplified than the one incorporated in the present model uses a friction coefficient c_D, yielding the drag

$$D_F = \frac{1}{2}\rho_1 c_D U^2 A, \tag{29}$$

where A is the cross-sectional area facing the flow. For the type of Gaussian obstacle described in section 3, this can be evaluated $A = \sqrt{\pi/2}lh_0$, making D_F normalized by $\rho_1 g' l h_0^2$ take the form

$$\frac{D_F}{\rho_1 g' l h_0^2} = \frac{1}{2}\left(\frac{\pi}{2}\right)^{1/2} c_D H_1'^{-1} M^{-1} \mathrm{Fr}^2, \tag{30}$$

where $M = h_0/H_1$ is the nonlinearity parameter, revealing a dependence proportional to Fr^2, which is consistent with what can be seen in the results with friction in Fig. 4.

The contrast of all the model results described above with those from 3D hydrostatic theory (dotted lines), which severely overestimate the drag for all $\mathrm{Fr} > 1$ and obviously underestimates it for $\mathrm{Fr} < 1$, is striking. Two-dimensional nonhydrostatic theory (dashed lines), on the other hand, severely overestimates the drag for $\mathrm{Fr} < 1$ and underestimates it for $\mathrm{Fr} \geq 1$, as would be expected.

Figures 4b,d,f shows that the agreement between theory and measurements is not as satisfactory for the higher obstacle B. As mentioned previously, the choice made to normalize the drag may not give the best scaling when nonlinear effects are important, as seems to happen here. Note also that the error bars in the experimental data are considerably smaller than in Figs. 4a,c,e owing to a larger signal-to-noise ratio in the measurements. The measured drag has a somewhat flatter distribution as a function of Fr and, hence, is more substantially overestimated at the maximum by all models and underestimated at low Fr (only one data point). The agreement between the model for $H_2 \to \infty$ without friction (dashed–dotted lines and stars) and measurements is more satisfactory for $\mathrm{Fr} > 1.3$ than that of the two-layer model with friction (solid lines and filled circles), apparently because frictional effects are being overestimated. This is consistent with the result that the normalized form drag given by (30) is inversely proportional to the dimensionless mountain height $M = h_0/H_1$ and is, hence, smaller for obstacle B (which has $M = 1.12$ on average) than for obstacle A (with $M = 0.66$ on average). This nonlinear effect cannot, however, be incorporated in the representation of friction adopted here other than by decreasing $\lambda\overline{H}/U$, which would necessarily also increase the predicted drag maximum, further degrading the agreement there.

Near the main drag maximum, the experimental data in Figs. 4b,d,f are substantially less overestimated by the discrete model data than by the continuous line obtained with averaged flow parameters, except for a few data points that are overestimated even more. In Fig. 4f, the average ratio between the theoretical and experimental values is 2.24, with a large contribution from the points with higher Fr. Among 28 data points available, the two-layer model with friction is within a factor of 2 of the data for 9 (32%) of these points and within a factor of 3 for 24 (86%) of them.

Again, 3D hydrostatic theory and 2D nonhydrostatic theory produce much worse agreement, with much more severe overestimation of the data for Fr $>$ 1 or Fr $<$ 1, respectively.

Differences between Figs. 4a,c,e and 4b,d,f can be largely attributed to nonlinear effects. Both Jiang and Smith (2000) and Johnson and Vilenski (2004) showed that these effects lead to an overestimation of the drag maximum as a function of Fr by linear theory (without friction) and an underestimation of the drag away from the maximum. However, Fig. 7 of Jiang and Smith (2000) shows a migration of the drag maximum to higher values of Fr as nonlinearity (quantified by M) increases. This does not explain the drag behavior seen in Fig. 4, described above. The numerical model used by Jiang and Smith (2000) was based on the shallow-water equations, so nonhydrostatic effects were not taken into account. This suggests that nonhydrostatic effects may be dominant over nonlinear effects to explain the value of Fr at which the maximum drag is attained in Fig. 4. Besides, Fig. 7 of Johnson and Vilenski (2004) shows a very substantial flattening of the drag distribution as a function of Fr [or, equivalently, with the related "detuning parameter," defined in their paper as $\Gamma = (\mathrm{Fr} - 1)M^{-2/3}$], which is qualitatively similar to what can be seen in Figs. 4b,d,f, although the nonlinearity is somewhat weaker here with $M = 1.12$ on average than in Fig. 7 of Johnson and Vilenski (2004), where $M = 2$. By comparison with that latter figure, the secondary drag maxima in Figs. 4a,c,e (at Fr $\approx$ 1.2–1.3) and in Figs. 4b,d,f (at Fr $\approx$ 1.5–1.6) might be interpreted as manifestations of solitary waves (which require both nonlinearity and nonhydrostatic effects to exist). However, the fact that both the two-layer model with friction and the model for $H_2 \to \infty$ without friction are able to somehow predict this secondary maximum in Figs. 4a,c shows that it can be attributed at least partly to the variation of l/H_1 between data points in the experiments with obstacle A.

Some speculative comments may be made on the role of nonlinear effects in these cases. Esler et al. (2007) developed a scaling for the drag as a function of the detuning parameter, showing from nonlinear theory that the drag maximum scales as $M^{5/3}$. In terms of the normalization used in Fig. 4, this means that the drag maximum should vary as $M^{-1/3}$. Since the maximum of the normalized drag in the data is about 0.40 for obstacle A (Figs. 4a,c,e), this would imply (assuming other parameters remained constant) a drag maximum of ~0.33 for obstacle B (Figs. 4b,d,f), which seems to agree qualitatively with the data (the maximum is actually 0.30). The linear prediction of the maximum in Figs. 4b,d,f is actually higher than in Figs. 4a,c,e because the flow is more hydrostatic (cf. Fig. 2) and obviously nonlinear effects are neglected. So, differences between Figs. 4a,c,e and 4b,d,f appear to be dominated by nonlinear effects. It should be noted, however, that the previous studies mentioned above used one-layer models, which is an obvious limitation.

The main conclusion to take from this comparison is that 3D and nonhydrostatic effects appear to explain the drag behavior observed in the experiments to a certain extent, accounting for the nonzero drag for Fr $<$ 1 and the migration of the drag maximum to Fr $<$ 1. Frictional effects act in the same direction. The effect of nonlinearity, which appears to be much stronger for obstacle B (Figs. 4b,d,f), consistent with the corresponding value of M, may explain the worse performance of the model in that case.

c. *Waves at the density interface*

It is useful to understand what kinds of waves are associated with each drag regime. Figure 5 presents the normalized streamline (or density interface) vertical displacement field at $z = H_1$ due to resonant waves given by (23), which is representative of density interfaces within the atmosphere or the ocean, for different values of Fr and l/H_1. The selected values of Fr (0.6, 0.8, 1.0, 1.2, 1.4, 1.6, and 1.8) have been chosen to encompass cases with both Fr $\leq$ 1 and Fr $\geq$ 1 and on both sides of the drag maxima shown in Fig. 2a. Figures 5a–d, 5e–h, 5i–l, and 5m–p present results for $l/H_1 = 1$, $l/H_1 = 2$, $l/H_1 = 5$, and $l/H_1 = \infty$, respectively, which correspond to flow that is strongly nonhydrostatic, intermediate, weakly nonhydrostatic, and perfectly hydrostatic.

In each row except Figs. 5m–p, as Fr increases, the resonant wake downstream of the obstacle shifts from being dominated by transverse waves, with phase lines almost perpendicular to the incoming flow, to being dominated by divergent waves, with crests and troughs making a smaller angle with the flow. For intermediate values of Fr where both types of waves are important, the well-known "Kelvin ship-wave" pattern can be seen (e.g., Figs. 5b,f). As would be expected, the magnitude of the wave disturbance peaks near the drag maximum: for Fr between 0.6 and 0.8 in Figs. 5a–d and for Fr $\approx$ 0.8 in Figs. 5e–h and 5i–l (in the hydrostatic situation of Figs. 5m–p the drag maximum is infinite and occurs at Fr = 1, as discussed previously). More specifically, the minimum in streamline elevation (corresponding to an interface depression) immediately downstream of $(x, y) = (0,0)$ appears to be roughly proportional to the drag, which makes sense, since the drag force is essentially caused by the thinning of the lower fluid layer associated with this minimum. The value of Fr for which each type of

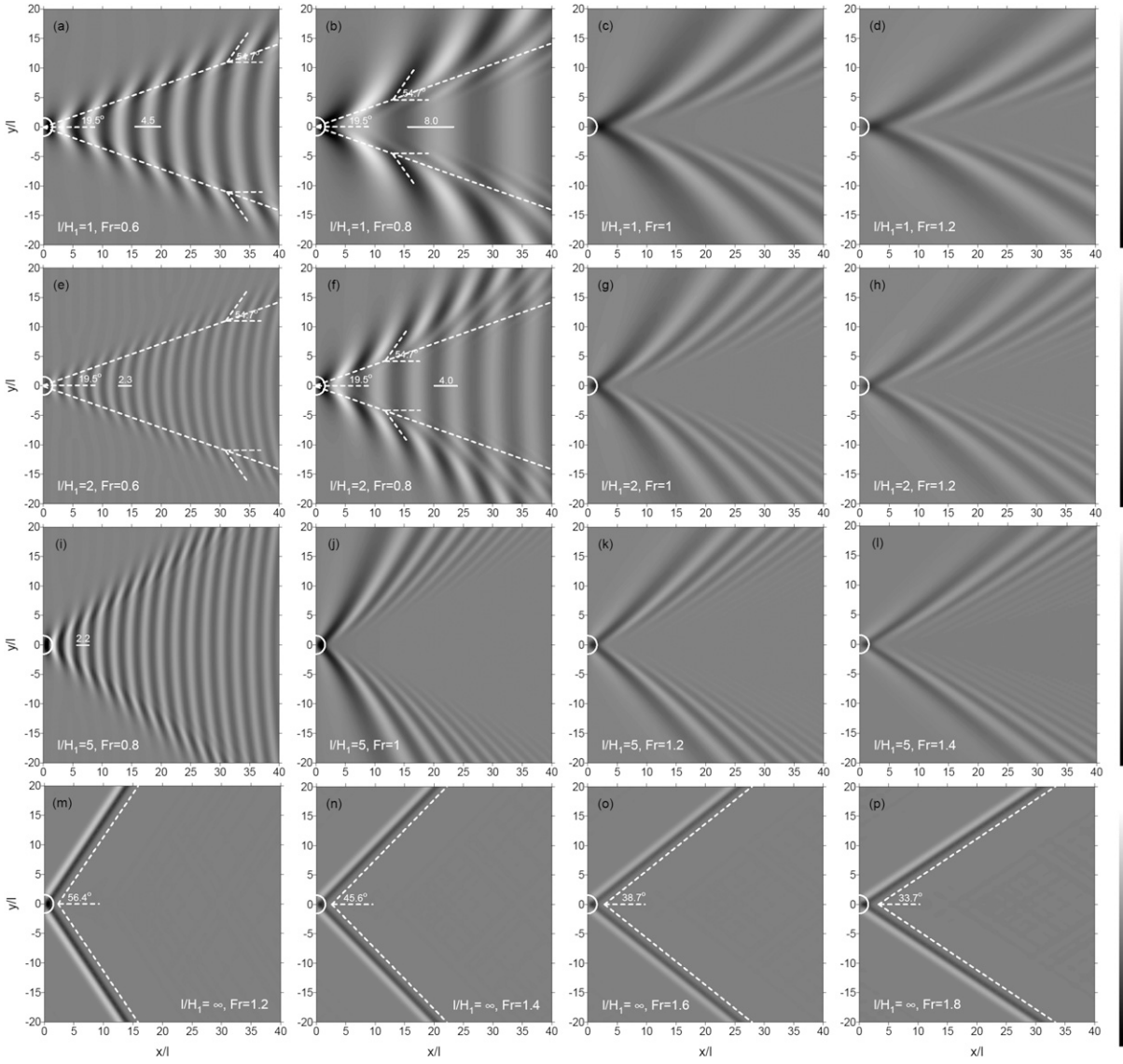

FIG. 5. Normalized vertical displacement of the streamlines (or density interface) at $z = H_1$ associated only with resonant or free stationary waves, $\eta_R(x, y)/h_0$, as a function of x/l and y/l, calculated from (23) (i.e., for $H_1/H_2 = 0$). (a)–(d) $l/H_1 = 1$, (e)–(h) $l/H_1 = 2$, (i)–(l) $l/H_1 = 5$, (m)–(p) $l/H_1 = \infty$. See legend for values of the Froude number used in each panel. The white circle centered at $(x = 0, y = 0)$ corresponds to the outline of the obstacle, drawn to scale, with $l = 32$ cm; that is, its normalized radius is 50 cm/32 cm ≈ 1.56 (see text). Solid white lines in (a),(b),(e),(f), and (i) denote predicted wavelengths. Dashed white lines show predicted wake angles. Scales on the right pertain to each row of graphs to their left.

waves occurs increases as l/H_1 becomes higher, which is consistent with the corresponding migration of the drag maximum to higher values of Fr closer to 1 in Fig. 2.

The relation between drag and interface depression can be made more quantitative by plotting the normalized drag as a function of the minimum of the interface elevation occurring immediately downstream of the obstacle, as shown in Fig. 6. This latter quantity was obtained from the η_R/h_0 field provided by (23) using a numerical iterative procedure. In this procedure, the minimum of η_R/h_0 is sought in the direction of the flow along the downstream portion of a line passing through the hill centerline. The process ends when a given threshold (10^{-6}) for the difference between the position of the minimum (expressed in terms of x/H_1) in consecutive iterations is reached. Figure 6 shows that there is a clear relationship between the drag and this minimum, which was fitted empirically using a power law (dotted line) expressed by

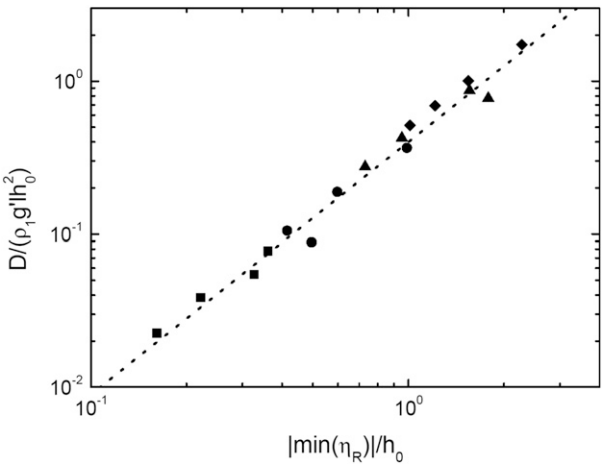

FIG. 6. Variation of the normalized drag with the normalized value of the minimum of the interface elevation occurring immediately downstream of the obstacle in the flows illustrated in Fig. 5. Each data point corresponds to one of the panels in that figure. Squares: $l/H_1 = 1$, circles: $l/H_1 = 2$, triangles: $l/H_1 = 5$, diamonds: $l/H_1 = \infty$. Dotted line: empirical fit to the data, expressed by (31).

$$\frac{D}{\rho_1 g' l h_0^2} = 0.40\left[\frac{|\min(\eta_R)|}{h_0}\right]^{1.65}. \tag{31}$$

Both the drag and the interface depression increase as l/H_1 increases, because the interface is able to interact more strongly with the topography. The fact that the power law in (31) is not linear accounts partly for the fact that the drag is a quadratic quantity, while the interface elevation is linear in the wave perturbations. The nonquadratic dependence and the scatter in the data points about the line account for the different locations along the hill slope where the η_R/h_0 minimum occurs, which affects the drag.

Some additional physical interpretation of the results can be obtained from (19), which gives the orientation angle of the resonant wavenumber vector θ_R (it must be kept in mind, however, that the definition of a wake angle is not trivial in the presence of both divergent and transverse waves). The function of κ' on the right-hand side of this equation decreases monotonically with its argument from 1 toward 0, which means that θ_R increases as both Fr and κ' increase. This implies that the angle of wave crests with the mean flow must decrease as either Fr or κ' increase (i.e., the wavelength decreases). These two aspects can be confirmed by Fig. 5 if one focuses on the orientation of the phase lines: it is visible not only that the crests of divergent waves become more aligned with the flow as Fr increases but also that the crests making the smallest angle correspond to the shortest waves (e.g., Figs. 5b–d and 5f–h). It also results from (19) that no transverse waves may exist if $\mathrm{Fr} > 1$, and even if they do exist at $\mathrm{Fr} = 1$, their wavelength is exceedingly large, and therefore impossible to detect, because $\kappa' \to 0$ is required. This is confirmed by Figs. 5c,d, 5g,h, and 5j,k.

A more thorough interpretation of the flow behavior requires more detailed analysis of the strongly nonhydrostatic (deep water) and nearly hydrostatic (shallow water) cases. In the strongly nonhydrostatic limit (19) reduces to

$$\cos^2\theta_R = \frac{\mathrm{Fr}^{-2}}{2\kappa'}, \tag{32}$$

from which it is easy to deduce the minimum wavenumber (or maximum wavelength $\lambda_{\max}$) of resonant waves, corresponding to wavenumber vectors aligned with the mean flow (transverse waves):

$$\frac{\lambda_{\max}}{H_1} = 4\pi\mathrm{Fr}^2. \tag{33}$$

This wavelength normalized by l instead of H_1 takes the values $\lambda_{\max}/l = 4.5$, 8.0, 2.3, and 4.0 for the cases displayed in Figs. 5a, 5b, 5e, and 5f, respectively. These values (marked in the corresponding graphs) provide a good prediction of the observed wavelengths of transverse waves for Figs. 5a and 5e, but underestimate them in Figs. 5b and 5f, probably because of shallow-water effects.

As is well known (e.g., Rabaud and Moisy 2013), the dispersiveness of nonhydrostatic waves allows the derivation of an upper bound for the wake angle. Using the fact that the group velocity of deep water waves is half of its phase velocity (a result that holds for the present interfacial wave case), it can be deduced that the angle of the wake made by waves of a given wavenumber is

$$\alpha(\kappa') = \arctan\left[\frac{(2\kappa'\mathrm{Fr}^2 - 1)^{1/2}}{4\kappa'\mathrm{Fr}^2 - 1}\right]. \tag{34}$$

This is found to attain a maximum of $\alpha_{\max} = 19.47°$ for a wavelength $\lambda = (2/3)\lambda_{\max}$, independently of Fr. This angle (marked in Figs. 5a,b,e,f) is in agreement with the wake angle seen in Figs. 5a and 5e, but the wake angle is larger in Figs. 5b and 5f, probably because of shallow-water effects in the excited waves, and also owing to the dominance of divergent waves, whose crests make a larger angle of 54.7° with the flow [determined from (32) and also marked in the same graphs]. The absence of transverse waves and the large wavelength of the leading

divergent waves make it difficult to determine the wake angle for $\mathrm{Fr} \geq 1$.

In weakly nonhydrostatic conditions (19) reduces to

$$\cos^2\theta_R = \frac{\mathrm{Fr}^{-2}}{1+\kappa'}, \tag{35}$$

which allows one to define a wake angle (in this case, simply as $\alpha = \pi/2 - \theta_R$ since nearly hydrostatic waves are almost nondispersive), given by

$$\alpha = \arcsin\left[\frac{\mathrm{Fr}^{-1}}{(1+\kappa')^{1/2}}\right] \tag{36}$$

from (35), and a maximum wavelength (again corresponding to transverse waves, which only exist if $\mathrm{Fr} \leq 1$) as

$$\frac{\lambda_{\max}}{H_1} = \frac{2\pi}{\mathrm{Fr}^{-2}-1}. \tag{37}$$

These two equations tell us that in the near-hydrostatic limit there is no upper bound for α when $\mathrm{Fr} \leq 1$, since (37) inserted into (36) always gives $\alpha = \pi/2$. However, angles near $\pi/2$ must be attained for very large wavelengths, which may not be easily discernible as waves (see, e.g., Fig. 5j). In the exact hydrostatic limit, dispersion ceases to exist and all wavenumbers are superposed spatially. In that limit, (36) reduces to $\alpha = \arcsin(\mathrm{Fr}^{-1})$, which although only valid for $\mathrm{Fr} > 1$, obviously decreases as Fr increases. This behavior can be clearly confirmed in Figs. 5m–p, and still with some dispersion due to nonhydrostatic effects in Figs. 5j–l. In this latter case, (37), which is only valid for $\mathrm{Fr} < 1$, gives a good estimate of the wavelength $\lambda_{\max}/l = 2.2$ (marked in the graph) for the transverse waves shown in Fig. 5i. In the former case, the values of Fr used in Fig. 5m–p (Fr = 1.2, 1.4, 1.6, and 1.8) yield $\alpha = 56.4°$, 45.6°, 38.7°, and 33.7°, respectively (marked in Figs. 5m–p), which are in good agreement with what is seen in the graphs.

It can be noticed that there are many qualitative similarities between the wave patterns displayed in Figs. 5a–l and in Fig. 8 of Lacaze et al. (2013); for example, there is a transition from the Kelvin ship-wave pattern to a wake dominated by divergent waves as Fr increases. A detailed comparison is beyond the scope of this article, but quantitative agreement seems less obvious. A reason for this could be that the shape to be taken into account in the theory to force the waves (using Fourier transforms) may not be exactly the topography shape itself. Instead the shape "seen" by the flow may include the effect of the boundary layer developing over the obstacle (Peng and Thompson 2003), which can separate from the topography under certain conditions or generate an upstream/downstream asymmetry, among other possibilities. However, this should in theory also affect the drag, which does not seem to occur, at least for obstacle A.

5. Discussion and conclusions

Theoretical calculations were developed for the drag force produced by an obstacle at the boundary of a stratified flow comprising two layers with different densities, owing to the generation of waves at the interface between them. The theoretical predictions were then tested using data from laboratory experiments. The conditions considered here are representative of either an atmosphere with a sharp temperature inversion at the top of the boundary layer flowing over an isolated hill, the motion of drifting ice keels at the surface of an ocean with a sharp thermocline, or an ocean flow with a sharp thermocline over a sill. The problem also has much in common with that of waves generated either at the thermocline or at the sea surface by ships (Grue 2015a; Moisy and Rabaud 2014), and their corresponding resistance force, which have been studied extensively. Results both from ship-wave theory (Rabaud and Moisy 2013) and from geophysical studies (e.g., Steeneveld et al. 2008) suggest that this gravity wave drag may be a substantial fraction of the total drag exerted on these obstacles. However its effect is usually neglected in a meteorological or oceanographic context (Lott and Miller 1997; Pite et al. 1995) and possibly misrepresented as turbulent form drag.

Two essential differences between the present study and the ship-wave problem are that the density discontinuity is much smaller than at an air–water interface (and can be in practice neglected except in the definition of buoyancy), hydrostatic (or shallow water) effects may be relevant, and the waves are generated remotely rather than at the same interface where the obstacle sits. The first difference allows us to use the Boussinesq approximation without substantial loss of accuracy. The second difference means that a theory for waves in a fluid of arbitrary depth must be used, which allows us to take both the "deep water" and the "shallow water" (hydrostatic) limits, the latter of which yields the hydrostatic drag expression from linear theory that was used in most previous studies. All of these differences are absent in the generation of waves by ships or ice keels at the thermocline, which is essentially similar to the problem being addressed here turned upside-down.

The drag estimated from laboratory experiments of a two-density-layer flow across an axisymmetric Gaussian

hill attains a maximum at a Froude number (Fr) slightly lower than 1 and is severely overestimated by 3D hydrostatic linear theory, which predicts the maximum to be infinite and exactly centered at Fr = 1. The experimental data are much better predicted by the 3D nonhydrostatic linear calculation developed here, in particular its two-layer version with a rigid lid including the effect of friction. However, even the model that is more directly applicable to the atmosphere, in which the upper layer is infinite and friction is neglected, produces much better results than hydrostatic theory. The inviscid two-layer version of the model provides an explicit expression for the drag in terms of a 1D integral. This expression shows that, for the conditions in the experiments, the drag depends essentially on three dimensionless parameters: Fr, the ratio of the obstacle width to the depth of the layer in contact with it; l/H_1, which quantifies nonhydrostatic effects; and the ratio of the thicknesses of the two fluid layers, H_2/H_1. An additional parameter of the flow, which is not taken into account in the model, is the nonlinearity parameter $M = h_0/H_1$. This model shows that a finite value of l/H_1 makes the drag maximum migrate to lower Fr and have its magnitude considerably reduced, markedly improving the agreement with experimental data compared to 3D hydrostatic linear theory or 2D nonhydrostatic linear theory, especially for the lower obstacle A used in the experiments. This suggests that the essential features of the drag behavior seen in the laboratory experiments, particularly for moderately steep orography, can be explained by nonhydrostatic effects, paving the way for the development of a simple parameterization of this process in atmospheric models. While the 3D nonhydrostatic linear results presented, for example, in Fig. 7 of Johnson and Vilenski (2004) or Fig. 3 of Grue (2015a) are byproducts and limit cases of their nonlinear nonhydrostatic models, the present study presents an explicit mathematical expression for this drag, which may be easily adapted for parameterization purposes.

Agreement with our 3D nonhydrostatic linear model, at least for obstacle A, may have been facilitated by the fact that the depths of the two fluid layers in the experiments are not equal. As noted by Johnson and Vilenski (2005) and Esler et al. (2007), this excludes cubic nonlinearities in the weakly nonlinear wave equation adopted by them, which can amplify the drag by a factor larger than 10 [see also Grue (2015b)]. Departures of the drag behavior from 3D nonhydrostatic linear theory, which are especially salient for the higher obstacle B considered in the experiments, are consistent with what is known from previous studies about the impact of nonlinearity on the flow—namely, causing a flattening of the drag variation with Fr.

The drag behavior in 3D nonhydrostatic linear theory is associated with characteristic wave signatures at the density interface. For $\mathrm{Fr} < 1$, and more precisely for an Fr lower than that where the drag maximum occurs, the flow is dominated by transverse waves with crests almost perpendicular to the flow, which are the only ones that exist in 2D nonhydrostatic conditions (where the drag is only nonzero for $\mathrm{Fr} < 1$). In contrast, when $\mathrm{Fr} > 1$ the flow is dominated by divergent waves, with crests at smaller angles to the flow, which are the only ones that exist in 3D hydrostatic flow (where the drag is only nonzero for $\mathrm{Fr} > 1$). When $\mathrm{Fr} \lesssim 1$ and l/H_1 is not too high, transverse and divergent waves coexist, forming a dispersive pattern strongly reminiscent of classical Kelvin ship waves, with a well-defined wake angle. The experimental results reported by Lacaze et al. (2013) are broadly qualitatively consistent with this structure of the wave pattern.

Feasible improvements to the 3D nonhydrostatic linear calculations developed here include a more accurate representation of friction—for example, using a bulk boundary layer approach akin to that developed by Smith et al. (2006) and Smith (2007). While in the data from laboratory experiments used here the boundary layer developed only over the obstacle, boundary layer influence on the drag may be more pervasive in the atmosphere—for example, when it is associated with the formation of rotors downstream of the obstacle (Teixeira 2017), which can substantially complicate the flow topology and lead to additional drag.

Part of the effect of the boundary layer is to modify the way the obstacle is ''seen'' by the flow, so that the actual shape to take into account in the theory is not the topography shape (Peng and Thompson 2003) but what the inviscid part of the atmosphere above ''sees.'' This is an important lead to improve both drag and wave-pattern predictions. Another feasible improvement would be considering the effects of stratification of the upper fluid layer, as in Teixeira et al. (2013) or Sachsperger et al. (2015).

Future work could include a combination of theory, numerical modeling, and laboratory experiments to explore further the combined influence of nonlinearity and nonhydrostatic effects. This could be based on the theoretical framework developed by Johnson and Vilenski (2005) and Esler et al. (2007), which includes weak nonlinearity and weak nonhydrostatic effects, or the more recent fully nonlinear framework developed by Grue (2015a, 2015b).

Acknowledgments. The authors acknowledge the financial support of the European Commission, under Marie Curie Career Integration Grant GLIMFLO,

Contract PCIG13-GA-2013-618016. The drag data used in this study came from experiments supported by the European Union's Sixth Framework Programme, through the budget of the Integrating Activity HYDRALAB III, Contract 022441(RII3), based upon an original idea of E. R. Johnson. METEO-FRANCE and CNRS also contributed significantly to the support of these experiments. We thank B. Beaudoin, B. Bourdelles, J.-C. Boulay, J.-C. Canonici, F. Murguet, M. Morera, S. Lassus Pigat, and H. Schaffner from the CNRM Geophysical Fluid Mechanics Laboratory in Toulouse for their kind support. We also thank F. Marie and F. Stoop for their help with data processing and S. Cazin, E. Cid, O. Eiff, J. G. Esler, O. Kryeziu, L. Lacaze, and J. D. Pearce for their participation in these experiments. We thank L. Lacaze and M. Mercier for a helpful discussion on wave pattern prediction. Finally we thank E. R. Johnson, who led the HYDRALAB III Transnational Access Project that supported the laboratory experiments used in this article.

APPENDIX

Complex Integration for Evaluating the Drag

The method to obtain (20) from (18) is outlined next. Taking the inner integral of (18), along θ

$$\int_0^{\pi/2} \frac{\kappa'^4 \cos^5\theta |\hat{h}'(\kappa')|^2}{\sinh^2(\kappa' H_1')\{\kappa' \cos^2\theta[\coth(\kappa' H_1') + \coth(\kappa' H_2')] - \mathrm{Fr}^{-2}\}} d\theta; \tag{A1}$$

this can be expressed generically as

$$\int_0^{\pi/2} \frac{f(\theta)}{g(\theta)} d\theta, \tag{A2}$$

where, in the present case,

$$\begin{aligned} f(\theta) &= \kappa'^4 \cos^5\theta |\hat{h}'(\kappa')|^2 / \sinh^2(\kappa H_1') \quad \text{and} \\ g(\theta) &= \kappa' \cos^2\theta[\coth(\kappa' H_1') + \coth(\kappa' H_2')] - \mathrm{Fr}^{-2}. \end{aligned} \tag{A3}$$

If there is no singularity in the integrand, the imaginary part of the integral (A1) is zero. If there is a singularity at θ_R within the interval $[0, \pi/2]$ [i.e., $g(\theta_R) = 0$], then, since the integrand is real, the imaginary part of the integral will only come from this singularity; namely,

$$\begin{aligned} \mathrm{Im}\int_0^{\pi/2} \frac{f(\theta)}{g(\theta)} d\theta &= \mathrm{Im}\left\{ \lim_{\varepsilon\to 0} \left[\int_{\theta_R-\varepsilon}^{\theta_R+\varepsilon} \frac{f(\theta)}{g(\theta)} d\theta \right] \right\} \\ &= \mathrm{Im}\left\{ \lim_{\varepsilon\to 0} \left[\frac{f(\theta_R)}{g'(\theta_R)} \int_{\theta_R-\varepsilon}^{\theta_R+\varepsilon} \frac{1}{\theta - \theta_R} d\theta \right] \right\} \\ &= \mathrm{Im}\left[\pm i\pi \frac{f(\theta_R)}{g'(\theta_R)} \right] = \pm\pi \frac{f(\theta_R)}{g'(\theta_R)}, \end{aligned} \tag{A4}$$

where $f(\theta)$ and $g(\theta)$ have been Taylor expanded around θ_R and the prime denotes differentiation with respect to θ. The sign can be elucidated by including friction in the problem. In the particular case under consideration, the minus sign must be chosen in (A4). Since

$$g'(\theta) = -2\kappa' \cos\theta \sin\theta[\coth(\kappa' H_1') + \coth(\kappa' H_2')], \tag{A5}$$

then

$$\begin{aligned} &\mathrm{Im}\left(\int_0^{\pi/2} \frac{\kappa'^4 \cos^5\theta |\hat{h}'|^2}{\sinh^2(\kappa' H_1')\{\kappa' \cos^2\theta[\coth(\kappa' H_1') + \coth(\kappa' H_2')] - \mathrm{Fr}^{-2}\}} d\theta \right) \\ &= \frac{\pi}{2} \frac{\kappa'^3 \cos^4\theta_R |\hat{h}'|^2}{\sinh^2(\kappa' H_1') \sin\theta_R [\coth(\kappa' H_1') + \coth(\kappa' H_2')]}. \end{aligned} \tag{A6}$$

If $\cos\theta_R$ and $\sin\theta_R$ are eliminated in (A6) using (19) and (A6) is inserted into the outer integral of (18), (20) is obtained.

A similar type of procedure, based on the original approach of Scorer (1949) but following more directly Sawyer (1962), may be used to obtain (23) from (8) and (14).

REFERENCES

Apel, J., J. Holbrook, A. Liu, and J. Tsai, 1985: The Sulu Sea internal soliton experiment. *J. Phys. Oceanogr.*, **15**, 1625–1651, doi:10.1175/1520-0485(1985)015<1625:TSSISE>2.0.CO;2.

Baines, P. G., 1995: *Topographic Effects in Stratified Flows*. Cambridge University Press, 498 pp.

Benzaquen, M., A. Darmon, and E. Raphaël, 2014: Wake pattern and wave resistance for anisotropic moving disturbances. *Phys. Fluids*, **26**, 092106, doi:10.1063/1.4896257.

Bordois, L., F. Auclair, A. Paci, Y. Dossmann, T. Gerkema, and C. Nguyen, 2016: Tidal energy redistribution among vertical modes in a fluid with a mid-depth pycnocline. *Phys. Fluids*, **28**, 101701, doi:10.1063/1.4964759.

Cummins, P. F., S. Vagle, L. Armi, and D. M. Farmer, 2003: Stratified flow over topography: Upstream influence and generation of nonlinear internal waves. *Proc. Roy. Soc. London*, **459A**, 1467–1487, doi:10.1098/rspa.2002.1077.

Dossmann, Y., A. Paci, F. Auclair, and J. W. Floor, 2011: Simultaneous velocity and density measurements for an energy-based approach to internal waves generated over a ridge. *Exp. Fluids*, **51**, 1013–1028, doi:10.1007/s00348-011-1121-3.

——, ——, ——, M. Lepilliez, and E. Cid, 2014: Topographically induced internal solitary waves in a pycnocline: Ultrasonic probes and stereo-correlation measurements. *Phys. Fluids*, **26**, 056601, doi:10.1063/1.4873202.

Esler, J. G., O. J. Rump, and E. R. Johnson, 2007: Non-dispersive and weakly-dispersive single-layer flow over an axysymmetric obstacle: The equivalent aerofoil formulation. *J. Fluid Mech.*, **574**, 209–237, doi:10.1017/S0022112006003910.

Farmer, D., and L. Armi, 1999: The generation and trapping of solitary waves over topography. *Science*, **283**, 188–190, doi:10.1126/science.283.5399.188.

Grue, J., 2015a: Nonlinear dead water resistance at subcritical speed. *Phys. Fluids*, **27**, 082103, doi:10.1063/1.4928411.

——, 2015b: Nonlinear interfacial wave formation in three dimensions. *J. Fluid Mech.*, **767**, 735–762, doi:10.1017/jfm.2015.42.

Hertenstein, R. F., 2009: The influence of inversions on rotors. *Mon. Wea. Rev.*, **137**, 433–446, doi:10.1175/2008MWR2482.1.

Hunt, J. N., 1964: The viscous damping of gravity waves in shallow water. *Houille Blanche*, **19**, 685–691, doi:10.1051/lhb/1964038.

Jiang, Q., and R. B. Smith, 2000: V-waves, bow shocks, and wakes in supercritical hydrostatic flow. *J. Fluid Mech.*, **406**, 27–53, doi:10.1017/S0022112099007636.

Johnson, E. R., and G. G. Vilenski, 2004: Flow patterns and drag in near-critical flow over isolated orography. *J. Atmos. Sci.*, **61**, 2909–2918, doi:10.1175/JAS-3311.1.

——, and ——, 2005: Two-dimensional leaps in the near-critical flow over isolated orography. *Proc. Roy. Soc. London*, **461A**, 3747–3763, doi:10.1098/rspa.2005.1530.

Knigge, C., D. Etling, A. Paci, and O. Eiff, 2010: Laboratory experiments on mountain-induced rotors. *Quart. J. Roy. Meteor. Soc.*, **136**, 442–450, doi:10.1002/qj.564.

Lacaze, L., A. Paci, E. Cid, S. Cazin, O. Eiff, J. G. Esler, and E. R. Johnson, 2013: Wave patterns generated by an axisymmetric obstacle in a two-layer flow. *Exp. Fluids*, **54**, 1618, doi:10.1007/s00348-013-1618-z.

Lin, Y.-L., 2007: *Mesoscale Dynamics*. Cambridge University Press, 674 pp.

Lott, F., and M. J. Miller, 1997: A new subgrid-scale orographic drag parametrization: Its formulation and testing. *Quart. J. Roy. Meteor. Soc.*, **123**, 101–127, doi:10.1002/qj.49712353704.

McFarlane, N. A., 1987: The effect of orographically excited gravity-wave drag on the general circulation of the lower stratosphere and troposphere. *J. Atmos. Sci.*, **44**, 1775–1800, doi:10.1175/1520-0469(1987)044<1775:TEOOEG>2.0.CO;2.

Moisy, F., and M. Rabaud, 2014: Scaling of far-field wake angle of non-axisymmetric pressure disturbance. *Phys. Rev.*, **89E**, 063004, doi:10.1103/PhysRevE.89.063004.

Nappo, C. J., 2012: *An Introduction to Atmospheric Gravity Waves*. 2nd ed. Academic Press, 359 pp.

Peng, M. S., and W. T. Thompson, 2003: Aspects of the effect on surface friction on flows over mountains. *Quart. J. Meteor. Soc.*, **129**, 2527–2557, doi:10.1256/qj.02.06.

Phillips, O. M., 1977: *Dynamics of the Upper Ocean*. Cambridge University Press, 337 pp.

Pite, H. D., D. R. Topham, and B. J. van Hardenberg, 1995: Laboratory measurements of the drag force on a family of two-dimensional ice keel models in a two-layer flow. *J. Phys. Oceanogr.*, **25**, 3008–3031, doi:10.1175/1520-0485(1995)025<3008:LMOTDF>2.0.CO;2.

Rabaud, M., and F. Moisy, 2013: Ship wakes: Kelvin or Mach angle? *Phys. Rev. Lett.*, **110**, 214503, doi:10.1103/PhysRevLett.110.214503.

——, and ——, 2014: Narrow ship wakes and wave drag for planing hulls. *Ocean Eng.*, **90**, 34–38, doi:10.1016/j.oceaneng.2014.06.039.

Sachsperger, J., S. Serafin, and V. Grubisic, 2015: Lee waves on the boundary layer inversion and their dependence on free-atmosphere stability. *Front. Earth Sci.*, **3**, 70, doi:10.3389/feart.2015.00070.

Sandu, I., A. Beljaars, P. Bechtold, T. Mauritsen, and G. Balsamo, 2013: Why is it so difficult to represent stably stratified conditions in numerical weather prediction (NWP) models? *J. Adv. Model. Earth Syst.*, **5**, 117–133, doi:10.1002/jame.20013.

Sawyer, J. S., 1962: Gravity waves in the atmosphere as a three-dimensional problem. *Quart. J. Roy. Meteor. Soc.*, **88**, 412–425, doi:10.1002/qj.49708837805.

Scorer, R. S., 1949: Theory of waves in the lee of mountains. *Quart. J. Roy. Meteor. Soc.*, **75**, 41–56, doi:10.1002/qj.49707532308.

——, 1953: Theory of airflow over mountains: II—The flow over a ridge. *Quart. J. Roy. Meteor. Soc.*, **79**, 70–83, doi:10.1002/qj.49707933906.

——, 1954: Theory of airflow over mountains: III—Airstream characteristics. *Quart. J. Roy. Meteor. Soc.*, **80**, 417–428, doi:10.1002/qj.49708034511.

Smith, R. B., 2007: Interacting mountain waves and boundary layers. *J. Atmos. Sci.*, **64**, 594–607, doi:10.1175/JAS3836.1.

——, Q. Jiang, and J. D. Doyle, 2006: A theory of gravity wave absorption by a boundary layer. *J. Atmos. Sci.*, **63**, 774–781, doi:10.1175/JAS3631.1.

Steeneveld, G. J., A. A. M. Holtslag, C. J. Nappo, B. J. H. V. de Wiel, and L. Mahrt, 2008: Exploring the possible role of small-scale terrain drag on stable boundary layers over land. *J. Appl. Meteor. Climatol.*, **47**, 2518–2530, doi:10.1175/2008JAMC1816.1.

Stensrud, D. J., 2009: *Parametrization Schemes: Keys to Understanding Numerical Weather Prediction Models*. Cambridge University Press, 459 pp.

Teixeira, M. A. C., 2014: The physics of orographic gravity wave drag. *Front. Phys.*, **2**, 43, doi:10.3389/fphy.2014.00043.

——, 2017: Diagnosing lee wave rotor onset using a linear model including a boundary layer. *Atmosphere*, **8**, 5, doi:10.3390/atmos8010005.

——, and C.-L. Yu, 2014: The gravity wave momentum flux in hydrostatic flow with directional shear over elliptical mountains. *Eur. J. Mech.*, **47B**, 16–31, doi:10.1016/j.euromechflu.2014.02.004.

——, J. L. Argaín, and P. M. A. Miranda, 2013: Orographic drag associated with lee waves trapped at an inversion. *J. Atmos. Sci.*, **70**, 2930–2947, doi:10.1175/JAS-D-12-0350.1.

Tuck, E. O., 1965: The effect of nonlinearity at the free surface on flow past a submerged cylinder. *J. Fluid Mech.*, **22**, 401–414, doi:10.1017/S0022112065000836.

Vosper, S. B., 2004: Inversion effects on mountain lee waves. *Quart. J. Roy. Meteor. Soc.*, **130**, 1723–1748, doi:10.1256/qj.03.63.

Wurtele, M. G., R. D. Sharman, and A. Datta, 1996: Atmospheric lee waves. *Annu. Rev. Fluid Mech.*, **28**, 429–476, doi:10.1146/annurev.fl.28.010196.002241.

Yu, C.-L., and M. A. C. Teixeira, 2015: Impact of non-hydrostatic effects and trapped lee waves on mountain-wave drag in directionally sheared flow. *Quart. J. Roy. Meteor. Soc.*, **141**, 1572–1585, doi:10.1002/qj.2459.